Some Examples of Local Electrical Characterization by Scanning Probe Microscopy

**Kyunghee Ryu, Sejin Kim, Yoojung Choi, Hyunjung Shin*,
Chan-Hyung Kim[1], Jung Bin Yun[2], and Bongki Lee[3]**

Center for Materials and Processes of Self-Assembly, School of Advanced Materials Engineering,
Kookmin University, Jeongneung-dong, Seongbuk-ku, Seoul 136-702, Korea
[1]Production Engineering Team 5, Dongbu Hitek, 474-1, Sangwoo-Ri,
Gamgok-Myeon, Eumseong-Gun, Chungcheongbuk-do 369-852, Korea
[2]Process Development Team 1, MagnaChip Semiconductor Ltd.
Hyangjeong-dong, Heungdeok-gu, Cheongju-si, Chungcheongbuk-do 361-728, Korea
[3]Department of Electrical Engineering, The University of Texas at Dallas,
P.O.#Box 830688, Richardson, TX 75083, USA

Various techniques of scanning probe microscopy, including Kevin probe force microscopy, scanning nonlinear dielectric microscopy, conducting atomic force microscopy and piezoresponse force microscopy, have proven to be powerful tools for local electrical characterization of various materials, such as metal, insulators and semiconductors. Use of these techniques is discussed with respect to methods of local electrical characterization and related principles on the surface of various materials.

Keywords: scanning probe microscopy, kevin probe force microscopy (KPFM), scanning nonlinear dielectric microscopy (SNDM), conducting atomic force microscopy (C-AFM)

1. INTRODUCTION

The material properties and physical processes that occur at the micrometer level down to the subnanometer level have been the main focus for many researchers during the past fifty years. Accordingly, scanning probe microscopy (SPM) has been developed for observation of the surface of materials on a fine scale. The first SPM technology was invented in 1981 by Gerd Binnig and Heinrich Rohrer at the IBM laboratory[1] as a form of scanning tunneling microscopy (STM), and its applications have increased exponentially in various fields of the physical sciences and engineering. In particular, the technology has highlighted the importance of nanoscale science and engineering.

In recent years, the rapid development of semiconductor industry has necessitated measurements of physical properties with nanometer-scale resolution on the surface of various electrical materials. SPM has been used to obtain geometrical as well as electrical information of materials with a high resolution for the purpose of enhancing the performance and circuit efficiency of devices. Many researchers have developed various SPM techniques such as the following: Kevin probe force microscopy (KPFM)[2], scanning

nonlinear dielectric microscopy (SNDM)[3,4], conducting atomic force microscopy (C-AFM)[5] and piezoresponse force microscopy (PFM)[6,7]. These techniques have proven to be a powerful tool for local electrical characterization. We now introduce some methods of local electrical characterization and present important results from various techniques of SPM (KPFM, SNDM, C-AFM, and PFM) with regard to the electrical characterization of the surface of various semiconductors.

2. EXPERIMENTAL PROCEDURE AND RESULTS

2.1. Kelvin Probe Force Microscopy

KPFM, which is also known as scanning surface potential microscopy, can use the electrostatic forces between a conducting tip and a sample to obtain surface potential through differences in the local work function. The work function is known to be influenced by many different physical processes: for example, the reconstruction of surfaces, adsorbed atoms and oxidation[8], the doping and band-bending[9] of semiconductors, and charge trapping in dielectrics[10]. A map of the work function produced by KPFM therefore provides local information about the electronic state of semiconductor surfaces. For instance, this technique has enabled study of the trapped charges in a nitride-oxide-silicon system[11], the silicon nanocrystals embedded in dielectric films[12], the

*Corresponding author: hjshin@kookmin.ac.kr

KPFM system
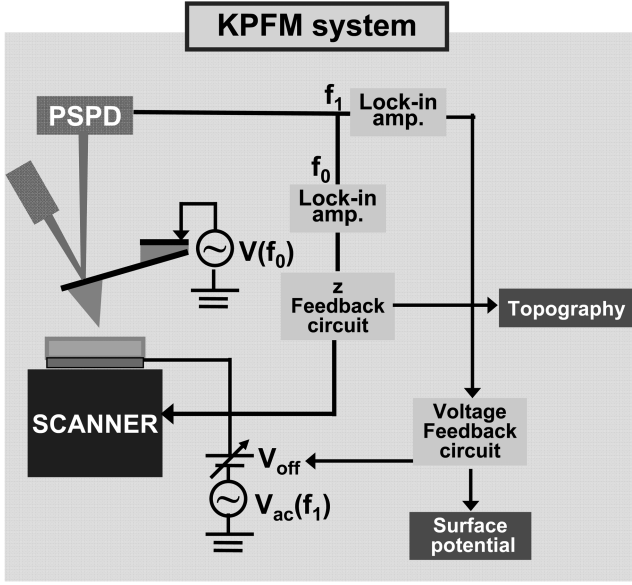
Fig. 1. Schematic diagram of the KPFM measurement setup. The f_0 signal is used to obtain topographic images, and the f_1 signal is used for surface potentials.

a) Sample	HOPG	Au	Pt	ITO
Literature work function (eV)	5.0	5.1~3	5.6~7	4.0~5.0
CPD (Tip-Sample) (V)	-0.45	-0.37	0.23	-0.15
Measurements work function (eV)	ref	5.08	5.68	5.3
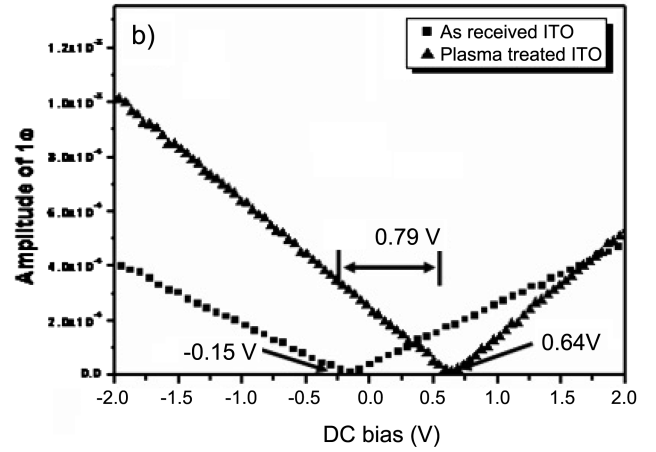
Fig. 2. (a) Measured work function on highly oriented pyrolytic graphite (HOPG), Au, Pt (111), and ITO films with an Au-coated tip; (b) measured work function of the as-received ITO and plasma-treated ITO.

dopant profile imaging of a p-n junction[13,14], photogenerated carrier diffusion to the junction[15], measurements of a local open-circuit voltage, and the photo-induced charging rates on a nanostructured organic solar cell[16].

Figure 1 shows a schematic diagram of the KPFM system. When the tip and sample are brought into contact, both the Fermi levels are aligned. Furthermore, the potential difference can be measured between two different materials, such as the tip and the sample. This measurement is called the contact potential difference (CPD). The CPD (ΔV) is therefore given by

$$\Delta V = \frac{\Phi_{tip} - \Phi_{sample}}{q}$$

Practically, to obtain the CPD, we applied ac and dc voltages between the tip and the sample. If we assume two conductors (the tip and sample) to be modeled as parallel capacitors, the electrostatic energy ($U = \frac{1}{2}CV^2$) is generated. Therefore, the attractive force, F, is induced as follows:

$$F = \frac{1}{2}\frac{\partial C}{\partial z}\Delta V^2$$

where C is the separation-dependent capacitance caused by the tip oscillation between the tip and a portion of the sample and z is the average tip-sample spacing. If any external mixed voltage ($V_{app} = V_{dc} + V_{ac}\sin wt$) is applied to the tip, the total electrostatic force between the two electrodes can be expressed as

$$F = \frac{1}{2}\frac{\partial C}{\partial z}(V_{app} - \Delta\Phi)^2$$

$$= \frac{1}{2}\frac{\partial C}{\partial z} + \left[(V_{ac} - \Delta\Phi)^2 + \frac{1}{2}V_{ac}^2\right](V_{ac} - \Delta\Phi)V_{ac}\sin(wt)$$

$$+ \frac{1}{4}\frac{\partial C}{\partial z}V_{ac}^2\cos(2wt) = F_0 + F_1\sin(wt) + F_2\cos(2wt)$$

The F_1 component depends on the surface contact potential between the tip and the sample, while the F_2 component depends on the ac voltage gradient of capacitance between the sample and the tip. Therefore, when F_1 is zero, that is the external dc voltage is equal to $\Delta\Phi$, the surface potential is obtained from the feedback loop modulation of the dc voltage to minimize the electrostatic force between the conducting tip and the sample.

To study how inductively coupled plasma with CF_4 gas influences the surface electronic structures of indium tin oxide (ITO) thin films, we used Kelvin probe force spectroscopy (KPFS)[17,18]. We also reported on the use of KPFM for the detection of electrons and holes in a nitride-oxide-silicon (NOS) system of flash memory. Our KPFS and KPFM measurements were performed under an ambient condition with
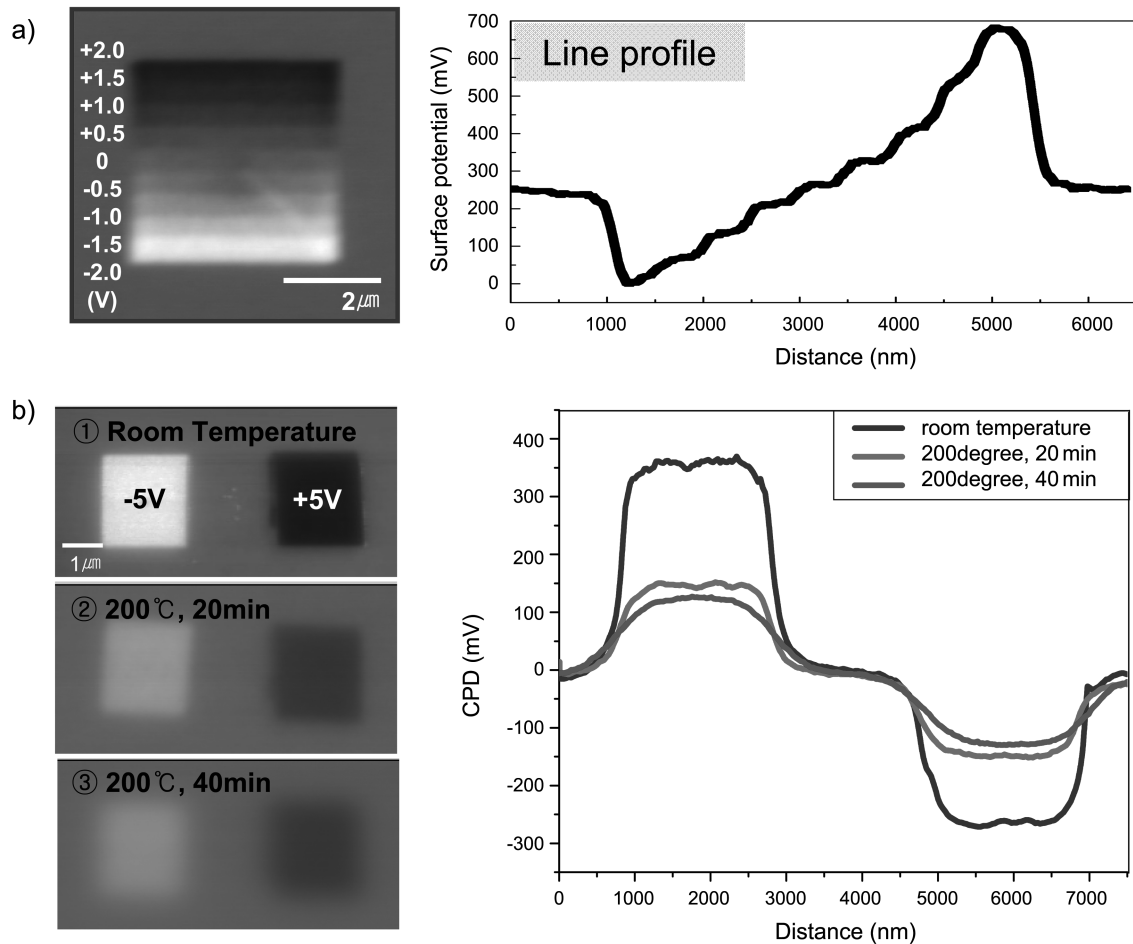
Fig. 3. (a) CPD images of negatively charged areas (-2 V/-1.5 V/-1.0 V/-0.5 V) and positively charged areas (0.5 V/1.0 V/1.5 V/2.0 V) in the SiO_2-Si_3N_4-SiO_2 film. (b) The left side of the figure: CPD images, from top to bottom, directly after application of a dc bias of -5 V and +5 V on the probe during the scanning of a 2 μm × 2 μm areas, after heating in a furnace for 20 min at 200°C and for 40 min at 200°C, respectively. The right side of the figure: a cross-sectional line profile.

a commercial AFM (SPA 400, SII, Japan), and we used gold-coated silicon cantilevers with a spring constant of ~3 N/m and a resonance frequency of 27 kHz.

To determine the work function of the ITO, we used KPFS for the measurements. Figure 2(a) shows the results with respect to a cantilever calibrated with highly oriented pyrolytic graphite (HOPG), Au, Pt (111), and ITO films. Figure 2(b) shows the CPD values of the as-received ITO and plasma-treated ITO. While the work function of the as-received ITO was 5.3 eV, the work function of the plasma-treated ITO was ~0.8 eV higher. There are two possible explanations for the increase in the work function of the plasma-treated ITO: First, the plasma treatment (energetic ion bombardment) creates a high number of surface defects, which generally produce surface states and bend the band upward. Second, the surface dipoles that form with the surface adsorption of O-species or F-species repel the free electrons in the conduction band, thereby leading to a surface depletion region and, consequently, an increase in the work function.

Figure 3 shows the KPFM images of the non-injected, the electron injected, and the hole-injected area in the NOS film. The nine 4.5 μm×0.5 μm rectangular regions were scanned by contact mode using conductive cantilever with the bias of -2.0, -1.5, -1.0, -0.5, 0, 0.5, 1.0, 1.5 and 2.0 V (from top to bottom) at the bottom electrode. The CPD induced by the electrons or holes trapped in the NOS structures was directly measured by KPFM. Figure 3(a) shows CPD images of the positively charged areas (-2.0 V/-1.5 V/-1.0 V/-0.5 V) and the negatively charged areas (0.5 V/1.0 V/1.5 V/2.0 V). The trapped charges in these 4.5 μm × 0.5 μm areas were injected with various bias conditions and their energy and density can be determined from the CPD induced by the trapped electrons or holes[11]. Figure 3(b) shows the spatial distribution of the tapped charges in the NOS system. The left-hand side of the figures shows the CPD images, from top to bottom, after the application of a dc bias of -5 V and +5 V on the probe for the scanning of an area of 2 μm×2 μm, after heating in a fur-

nace for 20 min at 200°C, and after heating in a furnace for 40 min at 200°C, respectively. The right-hand side of the figure shows a cross-sectional line profile. The CPD signal decreased vertically after heating in a nitrogen ambient condition, indicating that the trapped charges decayed mainly as a result of tunneling through the oxide layer.

2.2. Piezoresponse Force Microscopy

In recent years, researchers have expected ferroelectric materials to become the next-generation ultrahigh-density storage media because the domain wall thickness of typical ferroelectric materials is only a few lattices[19]. This focus of attention has necessitated fundamental studies of the ferro-

Fig. 4. Schematic diagram of the PFM measurement setup. The application of an alternating voltage generates vibrations in the ferroelectric sample, and conventional lock-in techniques are used to detect the vibrations as the first harmonic component of modulated cantilever deflection signal.

electric domain structures and their dynamics, particularly of the orientation effect on nanoscale polarization[20], the scaling limitation of ferroelectric switching[21], and the data retention characteristics of a nano-sized domain[22]. The recent development of a local piezoresponse measurement technique, namely PFM, has enabled nanoscale investigations of the ferroelectric domain. PFM can be used to observe the structure and dynamics of ferroelectric domains because an external ac voltage causes the ferroelectric sample to experience local electromechanical vibration. In order words, because all ferroelectric materials exhibit piezoelectricity, which is a linear coupling between the electrical and mechanical properties of a material, an electric field applied to a ferroelectric sample causes changes of its dimensions. Figure 4 shows a schematic diagram of the experimental setup for the PFM. The application of an alternating voltage generates vibrations in the ferroelectric sample, and these vibrations are detected with the aid of a conventional lock-in technique as the first harmonic component of the modulated cantilever's deflection signal. The amplitude (A) of the vibration signal (that is, the piezoresponse is defined as $A cos \Phi$ of the signal) provides information on the magnitude of the piezoelectric coefficient, while the phase signal (Φ) determines the direction of the polarization[23].

Our PFM measurements were performed under an ambient condition with a commercial AFM (SPA400, SII, Japan) equipped with a lock-in amplifier (Stanford Research Systems, SR830). The conductive tip was used as a movable top electrode. To minimize the electrostatic force interaction[23], we used platinum-coated silicon cantilevers with a high spring constant of ~5.5 N/m and length of 130 μm. During the PFM imaging, we applied a modulating voltage (V_{ac}) of 0.8 V (root mean square) and a frequency of 17 kHz to the bottom electrode while the tip was electrically grounded.
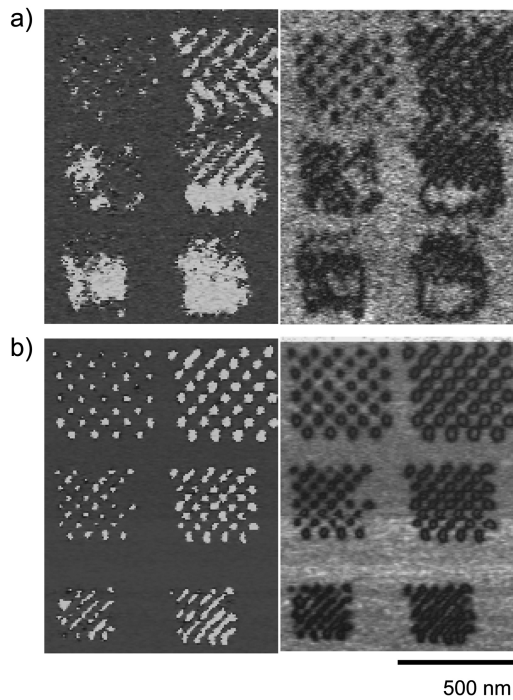
As shown in Fig. 5(a), we observed piezoresponse hysteresis loops of d_{33} vs. voltage to address the local switching characteristics of ferroelectric materials. We also demonstrated the
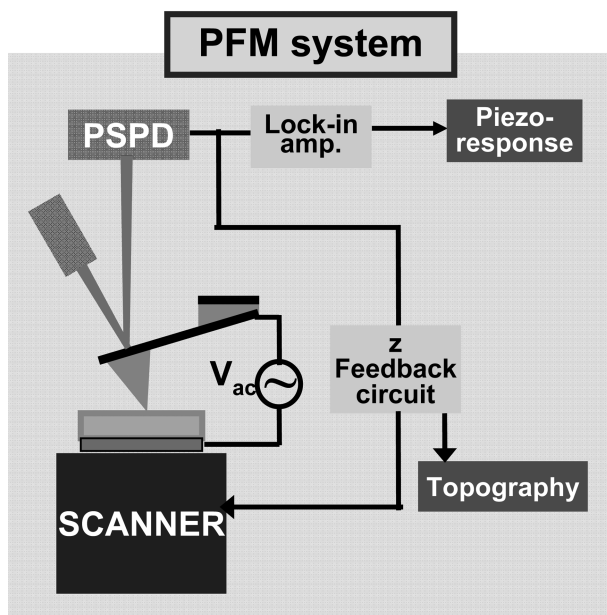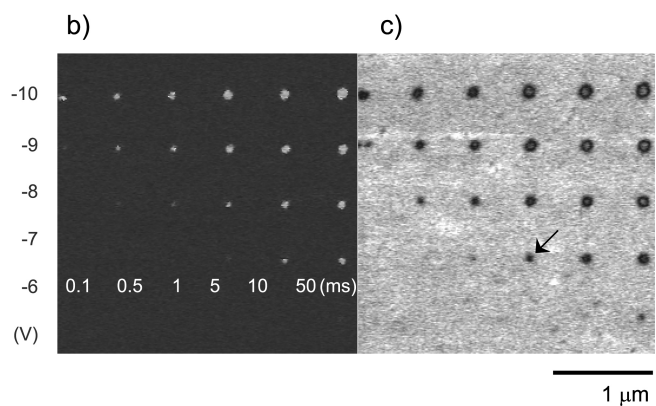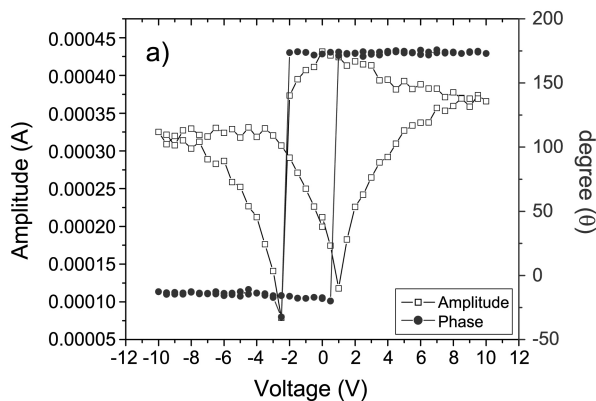

Fig. 5. (a) Piezoresponse hysteresis loops of d_{33} vs voltage; (b) the PFM amplitude; and (c) phase images. From top to bottom, the pulse amplitude was varied from -10 V to -5 V in 1 V steps; from left to right, the pulse duration was varied from 0.1 ms, 0.5 ms, 1 ms, 5 ms, 10 ms, and 50 ms.

Fig. 6. PFM amplitude and phase images of ferroelectric film with a thickness of (a) 60 nm and (b) 40 nm. An inverted domain dot array was performed equally under conditions of a pulse width (of 0.05 s and 0.5 s from left to right) and an amplitude (of +5 V and -5 V repeatedly).

size minimization of the ferroelectric domain with the applied voltage pulse amplitude and width, which was needed for the switch, and the stabilization of the induced domains by means of ferroelectric film with a thickness of 60 nm. Figures 5(b) shows the PFM phase images and Fig. 5(c) shows the amplitude images. From top to bottom in Figs. 5(b) and 5(c), the pulse amplitude varied from -10 V to -6 V in 1 V steps, and, from left to right, the pulse duration varied from 0.1 ms, 0.5 ms, 1 ms, 5 ms, 10 ms, and 50 ms. The smallest nanodomain dots that we obtained were 19 nm in diameter.

Using two different ferroelectric films, we generated inverted domain arrays, which can be used as arrays for storing information data bits, with an equal pulse width (of 0.05 s and 0.5 s from left to right) and an amplitude (of +5 V and -5 V repeatedly). We also produced arrays of inverted domain dots on a ferroelectric film (with a thickness of 60 nm); the dots had a diameter of 50 nm and a memory density of 256 Gbit/in^2. Furthermore, as shown in Fig. 6, we successfully arrayed individual dots with a diameter of 25 nm and a memory density of 1 Tbit/in^2 in a 40 nm thick ferroelectric film. These results indicate that the thinner ferroelectric film is more favorable for forming smaller data bits and, consequently, a higher memory density, most likely due to the inhomogeneous distribution of the electric field under the tip[24].
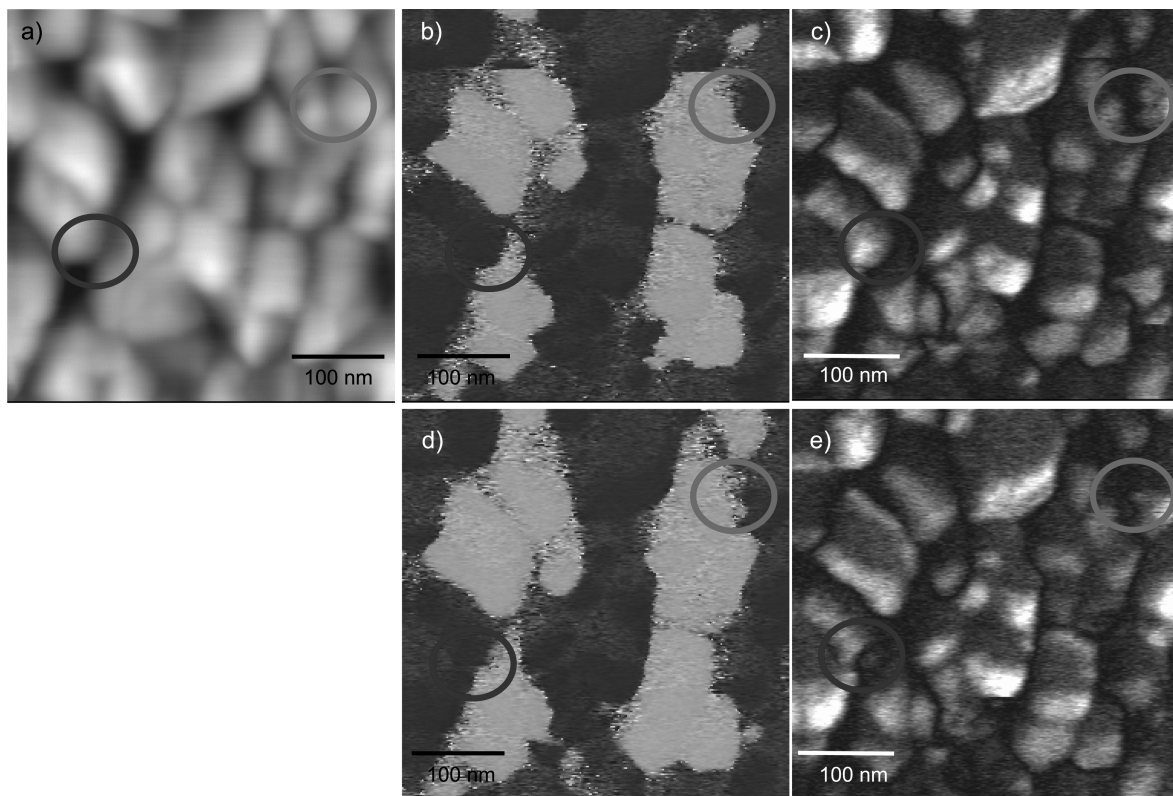
Fig. 7. Topography and PFM amplitude and phase images: (a) topography; (b) phase, (c) amplitude images after writing with a pulsed bias. (d) Phase and (e) amplitude images after 600 s in same area.

Figure 7 shows the domain wall dynamics in polycrystal-line ferroelectric thin films. Initially, back-poling was per-formed on an area of 1 μm×1 μm to induce upward
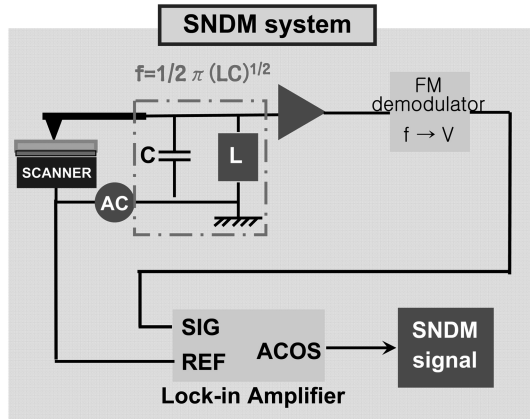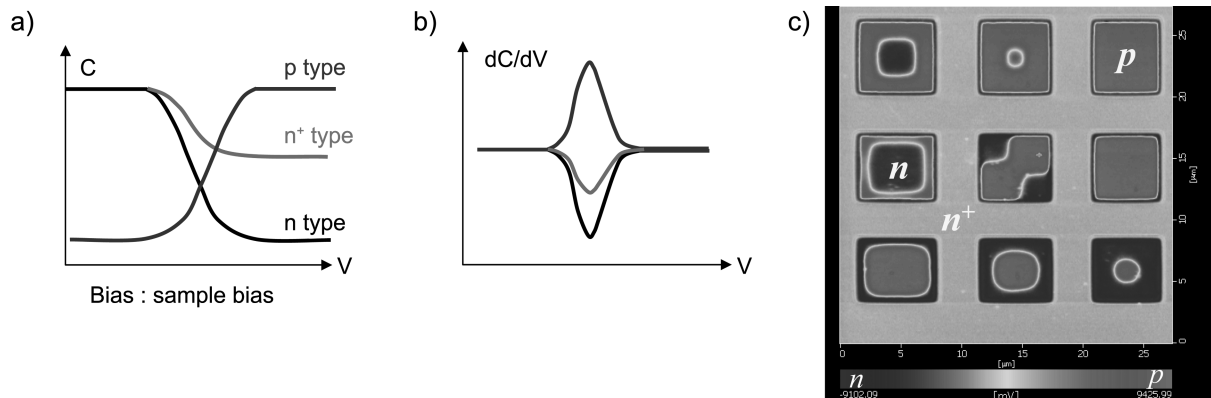

Fig. 8. Schematic diagram of the SNDM measurement setup. The capacitance variation resulting from the nonlinear dielectric response of the sample surface is detected as a change in the resonance fre-quency of the LC resonant circuit.

polarization at a bottom electrode voltage of +8 V. Then, we performed domain writing inside the back-poled area at pulse widths of 1 ms with a pulse amplitude of -8 V. Figures 7(a) to 7(e) show images of the topography, the PFM phase, and the amplitude. Figures 7(b) and 7(c) show phase and amplitude images directly after the writing with the pulsed bias, and Figs. 7(d) and 7(e) show the images taken after 600 s. The results confirm that spontaneous reversal can be initi-ated at the grain boundaries [25].

2.3. Scanning Non-linear Dielectric Microscopy

Since the first use of SCM by Matey and Blanc in 1984[26], SCM has evolved into a powerful characterization method for observation of carrier profiling in nanoscale semiconduc-tor structures with nondestructive techniques and high spa-tial resolution of sub-10 nm[27]. SNDM[3] proposed and developed a species of SCM, a technique for measurement of the changes in capacitance (dC/dV). Figure 8 shows a schematic diagram of the SNDM system. When the alternat-ing electric field is applied between the conductive tip and

Fig. 9. (a) Typical high frequency C-V curve in relation to the doping type and concentration; (b) the dC/dV signal; and (c) the SNDM signal of p-n structures.
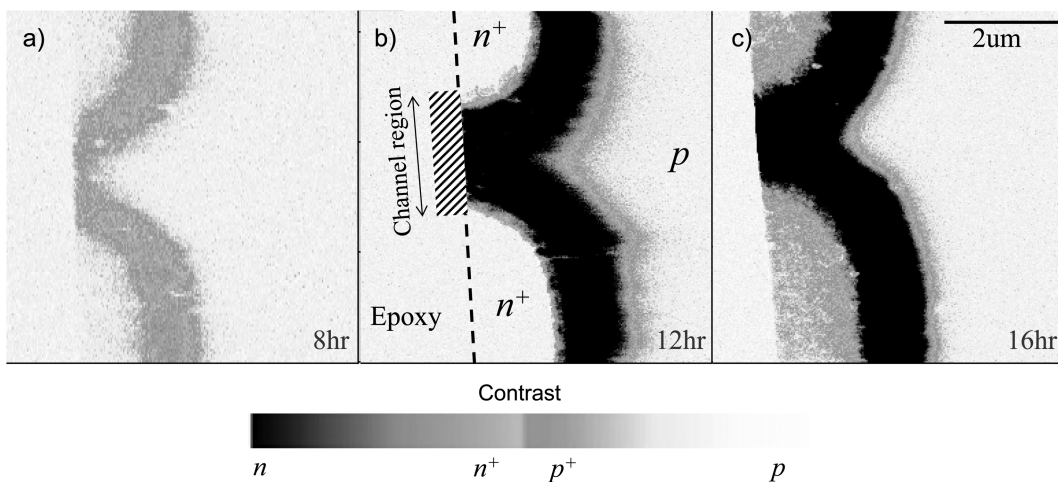

Fig. 10. Cross-sectional SNDM images in a channel width of 2 μm corresponding for the diffusion time of (a) 8 h, (b) 12 h, and (c) 16 h after the implantation of arsenic (As) ions into p-type silicon on an insulator wafer.

the sample, the capacitance variation resulting from the non-linear dielectric response of the sample surface can be detected as a change in the resonance frequency of an LC resonant circuit[28]. This method can help the following: visualization of the formation of a channel area between the source and the drain[29,30], the carrier density profile of dopants in implanted Si[31], the observation of electrons and holes in the SiO_2-Si_3N_4-SiO_2 film of flash memory[28,32], and the polarization switching images in ferroelectric thin films[33]. Figure 9(c) shows SNDM images of p-n structures. The p-n structures were fabricated through photolithography and ion implantation on highly doped n+-type Si with a density of 5×10^{19}/cm^3. The p-type regions were doped boron with a density of 2×10^{16}/cm^3, and arsenic was doped with a density of 13×10^{15}/cm^3 in the n-type region. Figure 9(a) shows a typical high frequency CV curve in relation to the doping type and concentration, and Fig. 9(b) shows the dC/dV signal. In SNDM, the capacitance mapping is constructed on the basis of the dC/dV signals. This type of mapping is clearly illustrated in Fig. 9(c), which shows that the dC/dV signal of the n-type region is negative whereas that of the p-type regions is positive.

Figures 10(a) to 10(c) show cross-sectional SNDM images with a channel width of 2 µm corresponding for diffusion time of (a) 8 h, (b) 12 h, and (c) 16 h after arsenic (As^+) ions were implanted into the p-type silicon on an insulator wafer. The SNDM measurements were performed under an ambient condition with a commercial AFM (SPA400, SII, Japan). We used a gold-coated silicon cantilever with a spring constant of ~1.6 N/m and a resonance frequency of 27 kHz. The applied ac voltage was 2 V and the applied dc voltage was 0 V. Figure 10 shows the n-type region in the channel region between the source and the drain. The n-type region formed as a result of the highly doped As region (n^+ type), which was formed by the annealing sequence. The SNDM results illustrate the successful formation of the n-type region in the channel region with the increasing annealing time.

2.4. Conducting Atomic Force Microscopy

The ability to measure the local electrical transport through insulating films or layers is essential for the development of useful nanoscale electronic devices. In contrast to STM, which can test only the conducting surface of materials, C-AFM can measure both the conducting and insulating electrical proper-
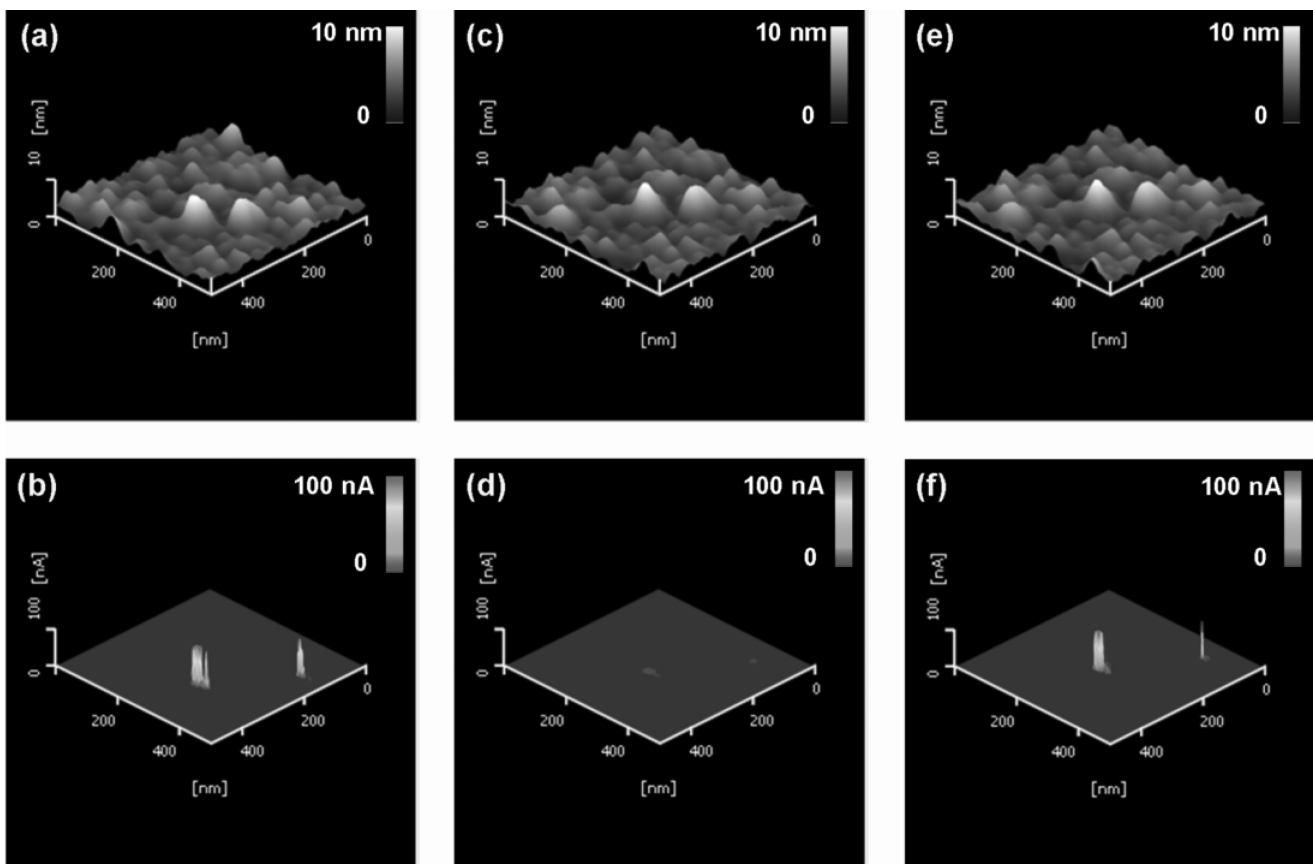
Fig. 11. Procedure of the repetitive switching cycle of the ultra-thin Pt/NiO/Pt layer, as measured by C-AFM. (a) and (b): the high conducting state was switched by a scan with a 2.3 V bias; (c) and (d): the low conducting state was switched by a scan with a 1.5 V bias; and (e) and (f): the high conducting state switched back again with 2.3 V. A scan voltage of 0.05 V for the conducting maps was chosen because that amount of voltage is sufficiently low to prevent any change during the measurement process.

ties of arbitrary samples. Thus, the local electrical characterization of conducting materials[5], the local photocurrent polymer/Fullerene solar cells[34], and the evolution of leakage paths in gate dielectrics[35] can be performed simultaneously with high lateral resolution and extreme sensitivity. We also demonstrate the ability of C-AFM to perform current mapping across of transition metal oxide films for potential bistable memory switching devices. We performed C-AFM by using Pt-coated Si cantilevers with a spring constant of 0.2 N/m. In the C-AFM measurements, a low tip-sample contact force was used to perform a nondestructive contact mode scanning procedure. The topography and current images were both obtained in ambient conditions.

The resistive memory switching phenomenon in transition metal oxides has attracted significant attention on account of its potential application for nonvolatile memories[36]. Using C-AFM, we visualized the localized and random formation of higher conducting areas (or spots) in nickel oxide films during repetitive switching. Figure 11 shows the higher conducting areas (or spots) in relation to the repetitive switching cycle of the ultra-thin layer of Pt/NiO/Pt. Some areas (or spots), which were assumed to be the beginning of the conducting filaments, appeared and disappeared in a localized and random fashion during the switching and are thought to contribute to resistive memory switching.

3. CONCLUSION

We have introduced various methods of local electrical characterization and fundamental studies of electrical characterization on the surface of various semiconductors by means of SPM (KPFM, SNDM, C-AFM, and PFM). The techniques of local electrical characterization by SPM are important for understanding the physical and electrical properties of nanoscale functional materials.

ACKNOWLEDGMENTS

REFERENCES

1. Gerd Binnig and Heinrich Rohrer, *Phys. Rev. Lett.* **49**, 57 (1982).
2. M. Nonnenmacher, M. P. O'Boyle, and H. K. Wickramasinghe, *Appl. Phys. Lett.* **58**, 2921 (1991).
3. Yasuo Cho, Akio Kirihara, and Takahiro Saeki, *Rev. Sci. Instrum.* **67**, 2297 (1996).
4. Yasuo Cho, Satoshi Kazuta, and Kaori Matsuura, *Appl. Phys. Lett.* **75**, 2833 (1999).
5. S. J. O'Shea, R. M. Atta, M. P. Murrell, and M. E. Welland, *J. Vac. Sci. Technol. B* **13**, 1945 (1995).
6. Sergei V. Kalinin and Dawn A. Bonnell, *Phys. Rev. B* **65**, 125408 (2002).
7. S. Hong, J. Woo, H. Shin, J. U. Jeon, Y. E. Pak, E. L. Colla, N. Setter, E. Kim, and K. No, *J. Appl. Phys.* **89**, 1377 (2001).
8. H. Sugimura, Y. Ishida, K. Hayashi, O. Takai, and N. Nakagiri, *Appl. Phys. Lett.* **80**, 1459 (2002).
9. A. Chavez-Pirson, O. Vatel, M. Tanimoto, H. Ando, H. Iwamura, and H. Kanbe, *Appl. Phys. Lett.* **67**, 3069 (1995).
10. G. Lubarsky, R. Shikler, N. Ashkenasy, and Y. Rosenwaks, *J. Vac. Sci. Technol. B* **20**, 1914 (2002).
11. S.-D. Tzeng and S. Gwo, *J. Appl. Phys.* **100**, 023711 (2006).
12. C. Y. Ng, T. P. Chen, H. W. Lau, Y. Liu, M. S. Tse, O. K. Tan, and V. S. W. Lim, *Appl. Phys. Lett.* **85**, 2941 (2004).
13. H. Shin, C. Kim, B. Lee, J. Kim, H. Park, D.-K. Min, J. Jung, S.-B. Hong, and S. Kim, *J. Vac. Sci. Technol. B* **24**, 2417 (2006).
14. H. Shin, B. Lee, C. Kim, H. Park, D.-K. Min, J. Jung, S. Hong, and S. Kim, *Electron. Mater. Lett.* **1**, 127-133 (2005).
15. T. Meoded, R. Shikler, N. Fried, and Y. Rosenwaks, *Appl. Phys. Lett.* **75**, 2435 (1999).
16. David C. Coffey and David S. Ginger, *Nature Mater.* **5**, 735 (2006).
17. C. Kim, B. Lee, H. J. Yang, H. M. Lee, J. G. Lee, and Shin, H. *J. Kor. Phys. Soc.* **47**, S417 (2005).
18. C. Kim, C. Bae, K. Ryu, B. Lee, and H. Shin, *Solid State Phenomena* **124-126**, 607 (2007).
19. B. Meyer and D. Vanderbilt, *Phys. Rev. Lett.* **65**, 104111 (2002).
20. Il-Doo Kim, Y. Avrahami, H. L. Tuller, Y.-B. Park, M. J. Dicken, and H. A. Atwater, *Appl. Phys. Lett.* **86**, 192907 (2005).
21. T. Tybell, C. H. Ahn, and J.-M. Triscone, *Appl. Phys. Lett.* **75**, 856 (1999).
22. J. Woo, S. Hong, D. K. Min, H. Shin, and K. No, *Appl. Phys. Lett.* **80**, 4000 (2002).
23. S. Hong, H. Shin, J. Woo, and K. No, *Appl. Phys. Lett.* **80**, 1453 (2002).
24. J. Woo, S. Hong, N. Setter, H. Shin, J.-U. Jeon, Y. E. Pak, and K. No, *J. Vac. Sci. Technol. B* **19**, 818 (2001).
25. A. Gruverman, H. Tokumoto, A. S. Prakash, S. Aggarwal, B. Yang, M. Wuttig, R. Ramesh, O. Auciello, and T. Venkatesan, *Appl. Phys. Lett.* **71**, 3492 (1997).
26. J. R. Matey and J. Blanc, *J. Appl. Phys.* **57**, 1437 (1985).
27. E. Bussmann and C. C. Williams, *Rev. Sci. Instrum.* **75**, 422 (2004).
28. K. Honda, S. Hashimoto, and Y. Cho, *Nanotechnol.* **16**, S90 (2005).
29. V. Raineri and S. Lombardo, *J. Vac. Sci. Technol. B* **18**, 545 (2000).
30. C. Kim, K. Ryu, H. Shin, B. Lee, H. Park, D.-K. Min, J. Jung, S.-B. Hong, and S. Kim, *Electron. Mater. Lett.* **2**, 151-156 (2006).

31. C. J. Kang, C. K. Kim, J. D. Lera, Y. Kuk, K. M. Mang, J. G. Lee, K. S. Suh, and C. C. Williams, *Appl. Phys. Lett.* **71**, 1546 (1997).

32. K. Honda and Y. Cho, *Appl. Phys. Lett.* **86**, 013501 (2005).

33. Y. Cho, S. Hashimoto, N. Odagawa, K. Tanaka, and Y. Hiranaga, *Appl. Phys. Lett.* **87**, 232907 (2005).

34. D. C. Coffey, O. G. Reid, D. B. Rodovsky, G. P. Bartho-lomew, and D. S. Ginger, *Nano let.* **7**, 738 (2007).

35. K. Kyuno, K. Kita, and A. Toriumi, *Appl. Phys. Lett.* **86**, 063510 (2005).

36. I. G. Baek, M. S. Lee, S. Seo, M. J. Lee, D. H. Seo, D.-S. Suh, J. C. Park, S. O. Park, H. S. Kim, I. K. Yoo, U-In Chung, and J. T. Moon, *IEDM Tech. Dig.* **04**, 587 (2004).